

# HoGS: Unified Near and Far Object Reconstruction via Homogeneous Gaussian Splatting

Xinpeng Liu<sup>1†</sup>   Zeyi Huang<sup>1†</sup>   Fumio Okura<sup>1</sup>   Yasuyuki Matsushita<sup>1,2</sup>  
<sup>1</sup>The University of Osaka   <sup>2</sup>Microsoft Research Asia – Tokyo  
 {liu.xinpeng, huang.zeyi, okura, yasumat}@ist.osaka-u.ac.jp

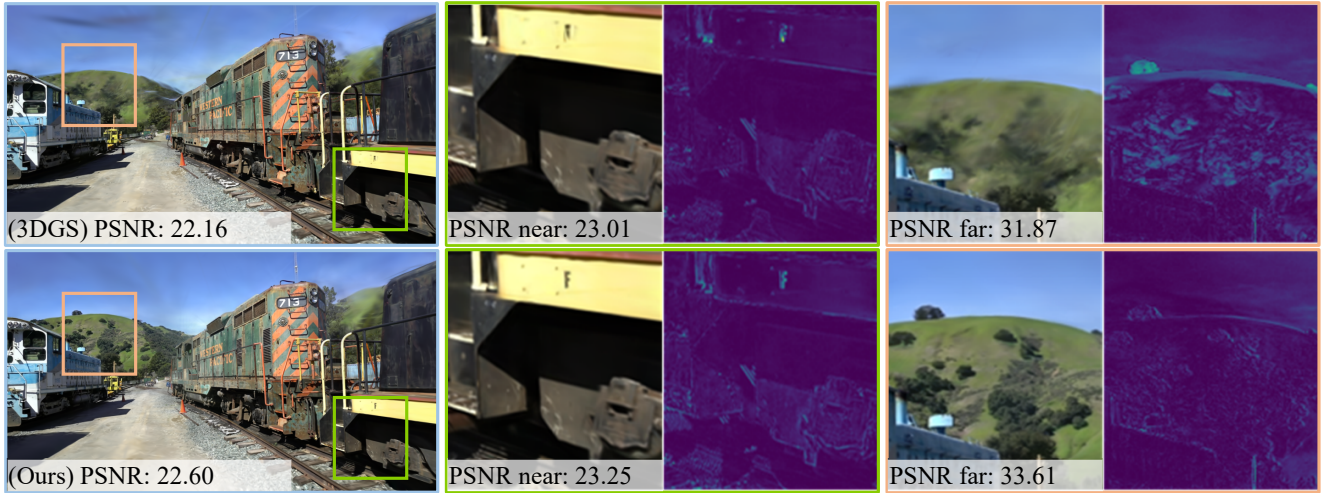


Figure 1. Homogeneous Gaussian Splatting (HoGS) uses homogeneous coordinates in the 3D Gaussian Splatting (3DGS) framework to represent both positions and scales. Homogeneous coordinates defined in the projective geometry represent nearby and distant objects seamlessly, thus our HoGS enables the accurate rendering of unbounded scenes while preserving the 3DGS’s fast training time and real-time performance. Compared to the traditional 3DGS, HoGS demonstrates improved robustness in capturing distant details while maintaining high fidelity in near-field objects.

## Abstract

Novel view synthesis has demonstrated impressive progress recently, with 3D Gaussian splatting (3DGS) offering efficient training time and photorealistic real-time rendering. However, reliance on Cartesian coordinates limits 3DGS’s performance on distant objects, which is important for reconstructing unbounded outdoor environments. We found that, despite its ultimate simplicity, using homogeneous coordinates, a concept on the projective geometry, for the 3DGS pipeline remarkably improves the rendering accuracies of distant objects. We therefore propose Homogeneous Gaussian Splatting (HoGS) incorporating homogeneous coordinates into the 3DGS framework, providing a unified representation for enhancing near and distant objects. HoGS effectively manages both expansive spatial positions and scales particularly in outdoor unbounded environments by adopting projective geometry principles. Ex-

periments show that HoGS significantly enhances accuracy in reconstructing distant objects while maintaining high-quality rendering of nearby objects, along with fast training speed and real-time rendering capability. Our implementations are available on our project page <https://kh129.github.io/hogs/>.

## 1. Introduction

Photorealistic scene reconstruction and novel view synthesis (NVS) have long been critical challenges in computer vision (CV) and computer graphics (CG). Implicit representations like neural radiance fields (NeRF) [14] use neural networks to model 3D scenes as continuous functions mapping spatial coordinates and viewing directions to color and density to synthesize views using volumetric rendering. These implicit methods have achieved groundbreaking performance in NVS but are limited by computationally intensive training and slow rendering processes. 3D Gaussian Splatting (3DGS) [7] addresses these limitations by intro-

<sup>†</sup> Authors contributed equally.

ducing an explicit representation of scenes using 3D Gaussians, which is compatible with rasterization, accelerating training and enabling real-time rendering.

Despite these advancements, generated images by 3DGS often contain blurred parts, particularly in surrounding environments in real-world unbounded scenes, such as clouds, distant mountains, and building clusters, as shown in Fig. 1. Due to perspective projection, large objects positioned far from the camera occupy only a tiny portion of the image plane. Unbounded scenes can span arbitrarily large regions in Euclidean space, making it challenging for 3DGS to optimize Gaussian kernels to distant positions while maintaining an observable size in Euclidean space.

Inspired by the concept of traditional projective geometry and homogeneous coordinates, we introduce the homogeneous coordinates into the 3D Gaussian representation. We further propose a new definition of Gaussian scales that complies with the concept of projective geometry. Our approach leverages the advantages of homogeneous coordinates over Cartesian coordinates in representing points at infinity, providing a smooth integration of Euclidean and projective spaces while handling nearby and distant points seamlessly and effectively. Compared to 3DGS, our method significantly improves the representation of distant objects while maintaining performance a comparably high performance for nearby regions as shown in Fig. 1.

Our contributions are twofold: first, we propose Homogeneous Gaussian Splatting (HoGS), a novel method adopting homogeneous coordinates to represent positions and scales of 3DGS for realistic and real-time rendering of both near and far objects. Second, despite the ultimate simplicity of HoGS, our method achieves state-of-the-art NVS results compared to other implicit and explicit representations.

## 2. Related Work

**Bounded View Synthesis.** We here refer to bounded view synthesis as the techniques that focus on scenes confined within a limited range [5]. All objects in the scene are within a bounded range relative to the camera, and there is no need to account for distant backgrounds.

Early NeRF methods rely on MLPs to approximate scene geometry and appearance by mapping spatial coordinates and viewing directions to density and color [14]. This volumetric approach supports high-detail, multi-view-consistent reconstructions but suffers from computational intensity, as MLPs must be evaluated across numerous sampled points along each camera ray, resulting in slow rendering and limited scalability for complex scenes [1, 12]. Various approaches accelerate rendering using thousands of smaller MLPs, as in KiloNeRF [17]. Techniques like InstantNGP [15] leverage multi-resolution hash tables for fast training and real-time rendering, albeit often with some sacrifice in image quality, particularly for high-resolution

scenes. Other improvements, such as reparameterization and optimized sampling, enhance fidelity by refining ray-marching accuracy [1, 19]. Despite these advancements, real-time applications remain limited by the inherent computational demands of volumetric ray-marching, a persistent bottleneck in implicit scene representations [4, 6].

3DGS [7] takes an explicit representation, *i.e.*, modeling 3D scenes with a set of anisotropic 3D Gaussians, and achieves high-quality results through rasterization rather than ray marching. Using alpha-blending and real-time rasterization, 3DGS avoids the computational burden of NeRF’s sampling strategies, producing fine details at real-time frame rates.

**Unbounded View Synthesis.** Several novel view synthesis studies particularly deal with unbounded views, *i.e.*, scenes without spatial constraints, encompassing central objects and vast, often distant, backgrounds [5].

Although implicit representations such as NeRF-based models have limitations in speed, they are effective in unbounded view synthesis by pairing specific scene types with appropriate 3D parameterizations. Several parameterization techniques for handling unbounded scenes are proposed so far. For instance, methods like NeRF++ [24], DONeRF [16], and Mip-NeRF 360 [2, 3] employ strategies called inverted sphere parameterization, radial distortion, and space contraction to model distant backgrounds, achieving realistic results despite increased computational costs. A more recent approach, Spherical Radiance Field (SRF) [5], uses spherical structures to capture unbounded environments with concentric representations efficiently.

In contrast to the implicit representations, explicit representations like 3DGS-based models are faster but face challenges in describing distant points in unbounded Euclidean space, which often have minimal parallax and fails to reconstruct sparse 3D points using the structure-from-motion (SfM) algorithm, which is often used as the initial positions of 3D Gaussians. To address this, some methods introduce spherical initial points to model far-off elements. Skyball [22] and skybox [8] use spherically mapped points for the sky and distant areas, based on segmentation between background and foreground. Similarly, Semantics-Controlled GS (SCGS) [18] uses scene boundaries by segmenting objects and distant areas in environments, allowing for applications such as sky replacement, while improving scene quality from diverse viewpoints. Scaffold-GS [13] employs anchor points and sparse point clouds to create a hierarchical 3D Gaussian scene representation, organizing the scene into regional anchor points and Gaussian nodes based on MLPs classifying scene types.

Unlike the existing methods, we achieve 3DGS-based unbounded view synthesis without pre-processing defining anchor points, sky regions, or scene segmentation but just by changing the 3DGS’s representation.

### 3. Methods

We propose HoGS, introducing the homogeneous projective geometry to 3DGS. We first summarize the 3D Gaussian Splatting in Cartesian coordinates [7], and then detail how we introduce homogeneous representations.

#### 3.1. Cartesian 3D Gaussian Splatting

3DGS using Cartesian coordinates is originally proposed by Kerbl *et al.* [7], representing scenes with 3D Gaussian primitives, which are rendered with a differentiable rasterization process. Each Gaussian primitive is characterized by its 3D mean  $\boldsymbol{\mu} \in \mathbb{R}^3$  and a covariance matrix  $\boldsymbol{\Sigma} \in \mathbb{R}^{3 \times 3}$ :

$$G(\mathbf{p}) = \exp\left(-\frac{1}{2}(\mathbf{p} - \boldsymbol{\mu})^\top \boldsymbol{\Sigma}^{-1}(\mathbf{p} - \boldsymbol{\mu})\right), \quad (1)$$

where  $\mathbf{p} \in \mathbb{R}^3$  denotes a point in the 3D Cartesian coordinates. The covariance matrix  $\boldsymbol{\Sigma}$  is decomposed into a scaling matrix  $\mathbf{S} = \text{diag}(s_1, s_2, s_3)$  and a rotation matrix  $\mathbf{R} \in \text{SO}(3)$  as

$$\boldsymbol{\Sigma} = \mathbf{R}\mathbf{S}\mathbf{S}^\top \mathbf{R}^\top. \quad (2)$$

In the 3DGS implementation, the scale and rotation are represented by a scaling vector  $\mathbf{s} = [s_1, s_2, s_3]^\top \in \mathbb{R}_{\geq 0}^3$  and the quaternion form  $\mathbf{q}$ , respectively. Both parameters are optimized independently in the pipeline along with the optimization of Gaussian appearances  $\{o, \mathbf{c}\}$  containing opacity and color represented as spherical harmonics.

**Optimization and Rendering.** To project 3D Gaussians to 2D, each Gaussian is transformed with the world-to-camera matrix  $\mathbf{T} \in \mathbb{R}^{3 \times 4}$  and a local affine transformation  $\mathbf{A} \in \mathbb{R}^{2 \times 3}$ , from which the variance matrix of 2D Gaussian is obtained. 3DGS then applies volumetric alpha compositing to generate the rendering results.

The parameters for each 3D Gaussian, *i.e.*,  $\{\boldsymbol{\mu}, \mathbf{s}, \mathbf{q}\}$  for geometry and  $\{o, \mathbf{c}\}$  for appearance, are optimized via the gradient descent approach to minimize a photometric loss combining  $\mathcal{L}_{\ell_1}$  and  $\mathcal{L}_{D-SSIM}$ , and the optimization pipeline cooperates with an adaptive densification control to make up for missing geometric features in rendering by populating Gaussians.

**A Challenge in Cartesian 3DGS.** Since the original 3DGS represents the Gaussians' position  $\boldsymbol{\mu}$  and scales  $\mathbf{s}$  in the Cartesian coordinates, it theoretically requires an infinite number of iterations to represent infinitely faraway or large objects via the gradient descent optimization. Besides, the change of position parameters  $\boldsymbol{\mu}$  causes the change of distance between the camera and the Gaussian primitive, affecting the size of Gaussians projected onto the image plane even if the scale parameters  $\mathbf{s}$  does not change. Practically, these phenomena prevent moving Gaussian primitives over large distances while preserving their shape reasonably on the projected image planes, making it difficult to reconstruct distant objects in scenes faithfully.

#### 3.2. Homogeneous Gaussian Splatting (HoGS)

We first briefly recap homogeneous coordinates, then describe how we reparametrize the position and scale of Gaussians using homogeneous coordinates.

**Homogeneous Coordinates.** Homogeneous coordinates in 3D extend Cartesian coordinates into a four-dimensional space, which allows for a more flexible representation of geometric translation, especially for projective geometry. Let a point  $\mathbf{p} = [x, y, z]^\top \in \mathbb{R}^3$  in 3D Cartesian coordinates is represented in projective space as  $\tilde{\mathbf{p}} = [\tilde{x}, \tilde{y}, \tilde{z}, w]^\top \in \mathbb{P}^3$  as

$$\tilde{\mathbf{p}} = \begin{bmatrix} \tilde{x} \\ \tilde{y} \\ \tilde{z} \\ w \end{bmatrix} = w \begin{bmatrix} x \\ y \\ z \\ 1 \end{bmatrix} \propto \begin{bmatrix} \mathbf{p} \\ 1 \end{bmatrix}. \quad (3)$$

The fourth element  $w$  is called the weight, which is often used for representing the translations and projections by a matrix-vector multiplication. Although not necessarily related to distance, the scaling by the weight  $w$  in the homogeneous coordinates accounts for depth, ensuring further points appear smaller and respecting real-world perspective. When  $w \neq 0$ , the homogeneous coordinates can be reduced to the Cartesian form  $[\frac{\tilde{x}}{w}, \frac{\tilde{y}}{w}, \frac{\tilde{z}}{w}]^\top \in \mathbb{R}^3$ . When  $w = 0$ , the homogeneous coordinates correspond to points at infinity, essential for representing vanishing points and lines in perspective views, which are fundamental in projective geometry. This makes homogeneous coordinates an effective representation in graphics, providing a consistent framework to handle perspective transformations.

Our HoGS is inspired by the advantages of homogeneous coordinates in handling perspective projection. Leveraging homogeneous coordinates' ability to seamlessly represent points regardless of their distance, we aim to improve the reconstruction quality for distant regions while preserving the high-quality rendering of near ones.

**Homogeneous Gaussians.** We here reparametrize not only positions but also scales of the Gaussian primitives in 3DGS using homogeneous coordinates. We consider the homogeneous coordinate system centered at the world origin  $O$ . Since an arbitrary 3D point in the homogeneous coordinate is given by Eq. (3), the 3D mean position of Gaussians can be rewritten in its homogeneous form  $\tilde{\boldsymbol{\mu}}$  as

$$\tilde{\boldsymbol{\mu}} = \begin{bmatrix} \boldsymbol{\mu} \\ w \end{bmatrix} \in \mathbb{P}^3 \propto \begin{bmatrix} \boldsymbol{\mu} \\ 1 \end{bmatrix}, \quad (4)$$

and the homogeneous mean  $\tilde{\boldsymbol{\mu}}$  can be converted to its Cartesian form simply by  $[\boldsymbol{\mu}, 1]^\top = \frac{\tilde{\boldsymbol{\mu}}}{w}$ .

To unify the representation of Gaussians' scaling with their positions in homogeneous coordinates, we newly introduce the concept of *homogeneous scaling*. For a Gaussian with the scaling vector  $\mathbf{s} = [s_1, s_2, s_3]^\top \in \mathbb{R}^3$ , we represent its scaling in homogeneous form as  $\tilde{\mathbf{s}} =$

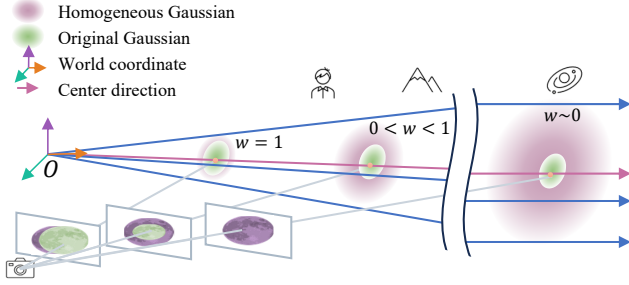


Figure 2. **Visualization of homogeneous Gaussians.** Our homogeneous coordinates are centered by the world origin  $O$ . Along the direction to the Gaussian (*i.e.*, center direction), the distance and size of each Gaussian primitive are controlled by homogeneous position  $\tilde{\mu} \in \mathbb{P}^3$  and scaling  $\tilde{s} \in \mathbb{P}^3$ . That is, even without changing the first three components in position  $\{\tilde{x}, \tilde{y}, \tilde{z}\}$  and scaling  $\{\tilde{s}_1, \tilde{s}_2, \tilde{s}_3\}$ , the Gaussian’s distance and scales change proportionally with its homogeneous component  $w$ . Following projective geometry principles, Gaussians further from the world origin  $O$  can have smaller  $w$  value to achieve proportionally larger scaling and maintain consistent projected dimensions at cameras enough close to the world origin  $O$  — a property not inherently ensured by the Cartesian 3DGS’s scaling definition. Using the homogeneous scaling allows for the relative scaling of Gaussians, accurately capturing the appearance of objects at large distances. This approach simplifies the optimization of scaling for distant objects, which are often not faithfully presented in the original 3DGS’s rendering.

$[\tilde{s}_1, \tilde{s}_2, \tilde{s}_3, w]^\top \in \mathbb{P}^3$ , sharing the same homogeneous component  $w$  as its position  $\tilde{\mu}$ . Specifically, we define the homogeneous scaling as:

$$\tilde{s} = \begin{bmatrix} \tilde{s}_1 \\ \tilde{s}_2 \\ \tilde{s}_3 \\ w \end{bmatrix} \in \mathbb{P}^3 \propto \begin{bmatrix} s_1 \\ s_2 \\ s_3 \\ 1 \end{bmatrix} = \begin{bmatrix} \mathbf{s} \\ 1 \end{bmatrix}, \quad (5)$$

where  $[\mathbf{s}, 1]^\top = \frac{\tilde{s}}{w}$  as the same manner to the positions.

Figure 2 illustrates the intuition of our HoGS unifying homogeneous position  $\tilde{\mu}$  and scales  $\tilde{s}$  of Gaussian primitives. By incorporating the same homogeneous component  $w$  into both the position and scaling vectors, we ensure that scaling operates within the same projective plane as the positions. This unified representation of position and scaling establishes a geometric framework that naturally guides the optimization of Gaussian parameters according to projective geometry principles. Similar to how the homogeneous component  $w$  in the position vector  $\tilde{\mu}$  relates to the distance from the world origin  $O$  and naturally represents points at infinity,  $w$  in the scale vector  $\tilde{s}$  naturally adjusts the Gaussians’ size with respect to the distance. As illustrated in the figure, even with the same position  $\{\tilde{x}, \tilde{y}, \tilde{z}\}$  and scaling  $\{\tilde{s}_1, \tilde{s}_2, \tilde{s}_3\}$  components, Gaussians can represent distant objects with small  $w \sim 0$ . From the cameras close enough to the origin  $O$ , Gaussians with different  $w$  are always projected to be the same size and position on the image plane.

In practice, these characteristics are useful for optimizing the scaling of objects with various depths, as homogeneous position and scaling represent the distance and size of primitives seamlessly. The model effectively learns object scaling that generalizes well across spatial depths, as further supported by the convergence analysis in Sec. 3.3 and the experimental results in Sec. 4.

**Optimization and Rendering.** In adaptive control of Gaussians, we turn off the functionality in the original 3DGS that large Gaussians in world space need to be periodically removed throughout the optimization, so that large Gaussians with distant positions can remain in scenes. The remaining part of the optimization and rendering pipelines are the same as the original 3DGS.

### 3.3. Convergence Analysis

Homogeneous coordinates represent both near and far points equivalently, offering a more consistent treatment across spatial positions and scales. This approach is expected to enhance optimization performance, while we here provide an empirical analysis of the convergence speed using a 1D synthetic setup. In detail, we optimize a specified point position relative to various target positions in a 1D space and analyze the convergence behavior of using homogeneous versus Cartesian coordinates. In this setup, the initial position is set to  $x = 5$ , which is also denoted as  $\tilde{x} = [\tilde{x} = 5, w = 1]^\top$  in its homogeneous coordinate. We set multiple target positions  $x_t$  (near:  $x_t = 10$ , intermediate:  $x_t = 50$ , and distant:  $x_t = 200$ ).

We optimize  $x$  and  $\tilde{x}$  in each representation to minimize the distance between the current and target position as

$$\begin{aligned} \text{Cartesian:} & \quad \mathcal{L}_c = |x_t - x|, \\ \text{Homogeneous:} & \quad \mathcal{L}_h = \left| x_t - \frac{\tilde{x}}{w} \right|, \end{aligned} \quad (6)$$

using the same learning rate. We observe both coordinate systems’ convergence rate and final error, training each for sufficient epochs to allow convergence. Figure 3 shows the results. Both representations similarly converge to the near target. However, for the intermediate and distant targets, the homogeneous representation achieved convergence in fewer iterations compared to the Cartesian representation.

## 4. Experiments

We perform both quantitative and visual comparisons using multiple datasets, as well as ablation studies.

### 4.1. Experiment Setup

**Implementation Details.** We implement our method with PyTorch and 3DGS’s CUDA kernels for rasterization. In our evaluation, we used the same hyperparameters in all scenes to ensure uniformity. All experiments were run on an RTX 8000 GPU for our method. Our method was trained

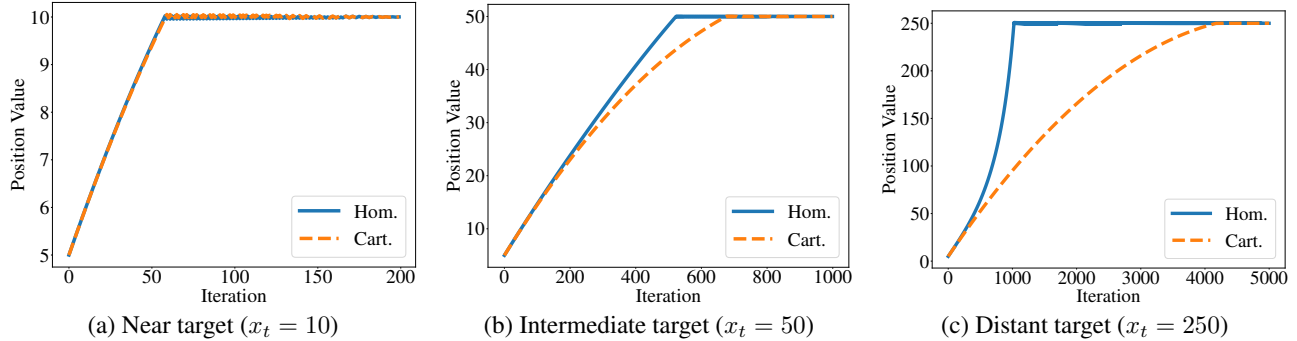


Figure 3. **Convergence analysis of homogeneous and Cartesian representation in 1D case.** We show a comparison of homogeneous and Cartesian representations’ optimization processes based on gradient descent in the 1D simulation. For a relatively near target, both representations are close in performance, while in other cases, the homogeneous representation is capable of converging at a faster speed.

for 50,000 iterations, and we adjusted densification-related hyperparameters to maintain the same as in the original 3DGS. We empirically set the learning rate of  $w$  to 0.0002. We assign the initial value of  $w$  concerning the distance  $d$  of each point from the world origin  $O$  by  $w = \frac{1}{d} = \frac{1}{\|P\|_2}$ , while we find that the initialization of  $w$  does not notably affect our method’s behavior, as described in our ablation study in Sec. 4.3. We use an exponential activation function for our new parameter  $w$  to obtain smooth gradients. To ensure the same behavior for position parameters, we apply the standard exponential decay scheduling for mean in 3DGS to  $w$ . We adopt the same hyperparameters and design choices as 3DGS in other parts.

**Datasets.** We evaluate the methods with 17 real scenes from multiple datasets. To ensure that the scenes contain diverse environments, we use both bounded indoor scenes and unbounded outdoor environments. In particular, we test our method on the full dataset of Mip-NeRF360 [2] including nine scenes containing four indoor and five outdoor scenes, two selected outdoor scenes from the Tanks&Temples dataset [9], as well as three indoor and three outdoor scenes from DL3DV benchmark [11] dataset.

To highlight the effectiveness of our method, we also want to evaluate the synthesis accuracy for near and far objects independently. Although it is difficult to determine the threshold of near and far scenes, we use Depth Anything V2 [21] to generate depth maps from the input images with original resolution. We define the farthest 5% of depth values in these maps as distant areas, and set a threshold accordingly. This evaluation is performed on unbounded scenes containing objects at varying depths, from the Tanks&Temples and DL3DV benchmark datasets.

**Metrics.** To perform consistent and meaningful error metrics analysis, we follow the methodology from Mip-NeRF 360 paper [2], using a train/test split for datasets and taking every eighth photo for testing. Following the practice of related literature, we downsample the images to the resolution

1.0–1.6K for a fair comparison, and use the standard SSIM, PSNR, and LPIPS metrics for performance measurement.

**Baselines.** Our HoGS is compared with recent NeRF-based and 3DGS-based methods to assess performance across different settings, namely INGP [15], Mip-NeRF 360 [2], Zip-NeRF [3], Scaffold-GS [13], and 3DGS [7].

Especially, Zip-NeRF [3] and Scaffold-GS [13], which are respectively based on NeRF and 3DGS, are considered as the representative baselines showing their state-of-the-art performance in unbounded outdoor scenes.

The results of INGP [15] on Mip-NeRF 360 and Tanks&Temples datasets are adopted from the previous publication of 3DGS [7]. We adopt the results of Mip-NeRF 360 [2] on their own dataset from the original paper. The rest of the results are generated from our run of each method’s official implementation with the NeRFBaselines [10] framework. For fair comparisons, all models input images with the same resolution. INGP, Mip-NeRF 360, and Zip-NeRF are tested using their default settings. 3DGS and Scaffold-GS are trained for 50,000 iterations, the same as ours, as we find that the larger iterations also gain their performance in unbounded scenes.

## 4.2. Results and Comparisons

We evaluated HoGS with several state-of-the-art techniques on NVS. Table 1 summarizes the quantitative comparison. It demonstrates that our HoGS achieves the best rendering quality among 3DGS-based methods in most cases.

Compared with the rendering performance of the qualitative state-of-the-art NeRF-based method (*i.e.*, Zip-NeRF), our method often achieves comparable results and sometimes outperforms in metrics. Zip-NeRF requires a longer training time of an average three hours (on four A6000 GPUs), compared to 40–60 min training by ours (on a single RTX 8000 GPU). Since we use the same CUDA kernel to the original 3DGS, our HoGS achieves almost the same training time to 3DGS under the same number of epochs and real-time rendering.

Dataset		Mip-NeRF 360 Dataset			Tanks&Temples			DL3DV-10K Benchmark		
Method	/ Metric	SSIM <sup>↑</sup>	PSNR <sup>↑</sup>	LPIPS <sup>↓</sup>	SSIM <sup>↑</sup>	PSNR <sup>↑</sup>	LPIPS <sup>↓</sup>	SSIM <sup>↑</sup>	PSNR <sup>↑</sup>	LPIPS <sup>↓</sup>
NeRF-based	INGP [15]	0.699	25.59	0.331	0.745	21.92	0.305	0.816	26.38	0.235
	Mip-NeRF 360 [2]	0.792	27.69	0.237	0.763	22.23	0.255	0.872	28.70	0.152
	Zip-NeRF [3]	0.829	28.56	0.187	0.840	23.64	0.151	0.930	30.91	0.084
3DGS-based	3DGS (50K iter) [7]	0.821	27.65	0.212	0.845	23.83	0.183	0.900	28.47	0.143
	Scaffold-GS (50K iter) [13]	0.825	28.08	0.206	0.854	24.31	0.169	0.902	29.11	0.137
	HoGS (Ours)	0.828	27.92	0.194	0.858	24.27	0.166	0.919	29.93	0.114

Table 1. **Quantitative comparison of novel view synthesis results.** According to the quantitative metrics, *i.e.*, SSIM, PSNR, and LPIPS, our ultimately simple method (HoGS) achieves the best performance among 3DGS-based methods in most cases. The rendering accuracy is comparable to Zip-NeRF [3], which shows state-of-the-art accuracy but requires time-consuming training and rendering.

Method	Mip-NeRF360 (Indoor)			Mip-NeRF360 (Outdoor)		
	SSIM <sup>↑</sup>	PSNR <sup>↑</sup>	LPIPS <sup>↓</sup>	SSIM <sup>↑</sup>	PSNR <sup>↑</sup>	LPIPS <sup>↓</sup>
Mip-NeRF 360	0.917	31.72	0.180	0.691	24.47	0.283
Zip-NeRF	0.929	32.33	0.161	0.748	25.54	0.209
3DGS	0.929	31.24	0.169	0.734	24.78	0.246
Scaffold-GS	0.934	31.79	0.160	0.738	25.11	0.243
HoGS (Ours)	0.930	31.38	0.163	0.747	25.14	0.219

Method	Tanks&Temples (Near)			Tanks&Temples (Far)		
	SSIM <sup>↑</sup>	PSNR <sup>↑</sup>	LPIPS <sup>↓</sup>	SSIM <sup>↑</sup>	PSNR <sup>↑</sup>	LPIPS <sup>↓</sup>
Mip-NeRF 360	0.800	23.30	0.207	0.966	30.47	0.047
Zip-NeRF	0.873	25.07	0.117	0.969	30.41	0.034
3DGS	0.881	25.64	0.140	0.966	29.40	0.042
Scaffold-GS	0.885	25.87	0.132	0.971	30.54	0.037
HoGS (Ours)	0.883	25.69	0.135	0.976	30.77	0.031

Method	DL3DV-10K (Near)			DL3DV-10K (Far)		
	SSIM <sup>↑</sup>	PSNR <sup>↑</sup>	LPIPS <sup>↓</sup>	SSIM <sup>↑</sup>	PSNR <sup>↑</sup>	LPIPS <sup>↓</sup>
Mip-NeRF 360	0.883	29.25	0.133	0.991	39.96	0.016
Zip-NeRF	0.939	31.56	0.071	0.993	41.45	0.011
3DGS	0.918	29.73	0.115	0.985	36.46	0.025
Scaffold-GS	0.912	29.80	0.118	0.991	39.01	0.016
HoGS (Ours)	0.927	30.53	0.098	0.993	40.55	0.013

Table 2. **Comparisons for indoor/outdoor and near/far scenes.** For Tanks&Temples and DL3DV-10K datasets, our HoGS shows remarkably better accuracy than other 3DGS-based methods for far scenes and also improves the near scene rendering. For Mip-NeRF 360 [2] indoor and outdoor scenes, HoGS shows strong results for general outdoor scenes, reaching close to the time-consuming Zip-NeRF.

The qualitative analysis in Fig. 4 visually presents our advantages in rendering the quality of our method. We can see that our method reconstructs distant details, which are usually missing in 3DGS results. Furthermore, in most cases, our method preserves a comparable level of detail for objects close to the view as in 3DGS and Zip-NeRF.

**Near/far and Indoor/outdoor Analyses.** We conducted detailed evaluations focusing on near and far regions (for Tanks&Temple and DL3DV datasets) or indoor and outdoor scenes (for the Mip-NeRF360 dataset) as summarized in Table 2. Our HoGS demonstrates remarkably superior performance over 3DGS-based methods in representing objects across depth ranges. Notably, without explicitly exploiting scene structural information, HoGS outperforms Scaffold-GS in both near and far regions. The results for Mip-

$w$	$1/d$	Random	0.01	0.1	1.0	10.0	100.0
SSIM <sup>↑</sup>	0.828	0.756	0.782	0.814	0.820	0.808	0.797
PSNR <sup>↑</sup>	22.60	21.63	21.78	22.38	22.52	22.33	22.16
LPIPS <sup>↓</sup>	0.191	0.281	0.241	0.204	0.204	0.225	0.240

Table 3. Ablation experiment for different initial values of  $w$ .

NeRF360 outdoor scenes indicate our method’s strength in general outdoor scenes. Our method achieves comparable or sometimes better results to Zip-NeRF in far regions, while maintaining a competitive performance in reconstructing near objects.

Figure 5 presents a visual comparison for near and far scenes, respectively. HoGS’s performance is impressive in reconstructing distant background objects, preserving both geometric accuracy and detail clarity.

### 4.3. Ablation Study

**Effect of Homogeneous Scaling.** In our method, homogeneous scaling is essential for maintaining accurate representations of near and distant objects. As shown in Fig. S6, although homogeneous representation allows our method to learn distant Gaussian positions, it is difficult for our method to learn the accurate shape of distant objects, which seem less defined in the example.

**Pruning of Large Gaussians.** We verify the effectiveness of our modified pruning strategy for Gaussians, which allows large Gaussians in world space. In our method, distant textureless regions can be represented with large Gaussians with reasonably far positions. However, with the original pruning strategy, such large Gaussians will be removed from the scene. As a result, the method will optimize for nearby floaters to represent such regions as in Fig. 7.

**Initialization of the Weight  $w$ .** To analyze the sensitivity of parameter  $w$  to its initial value, we experimented with different initialization values for  $w$  within the range of 0.01 to 100 and a randomly chosen value, as shown in Table 3. The results indicate negligible variation across PSNR, SSIM, and LPIPS metrics, suggesting that the initialization of  $w$  has a limited impact on output quality. This robustness arises from the nature of homogeneous coordinates: a single

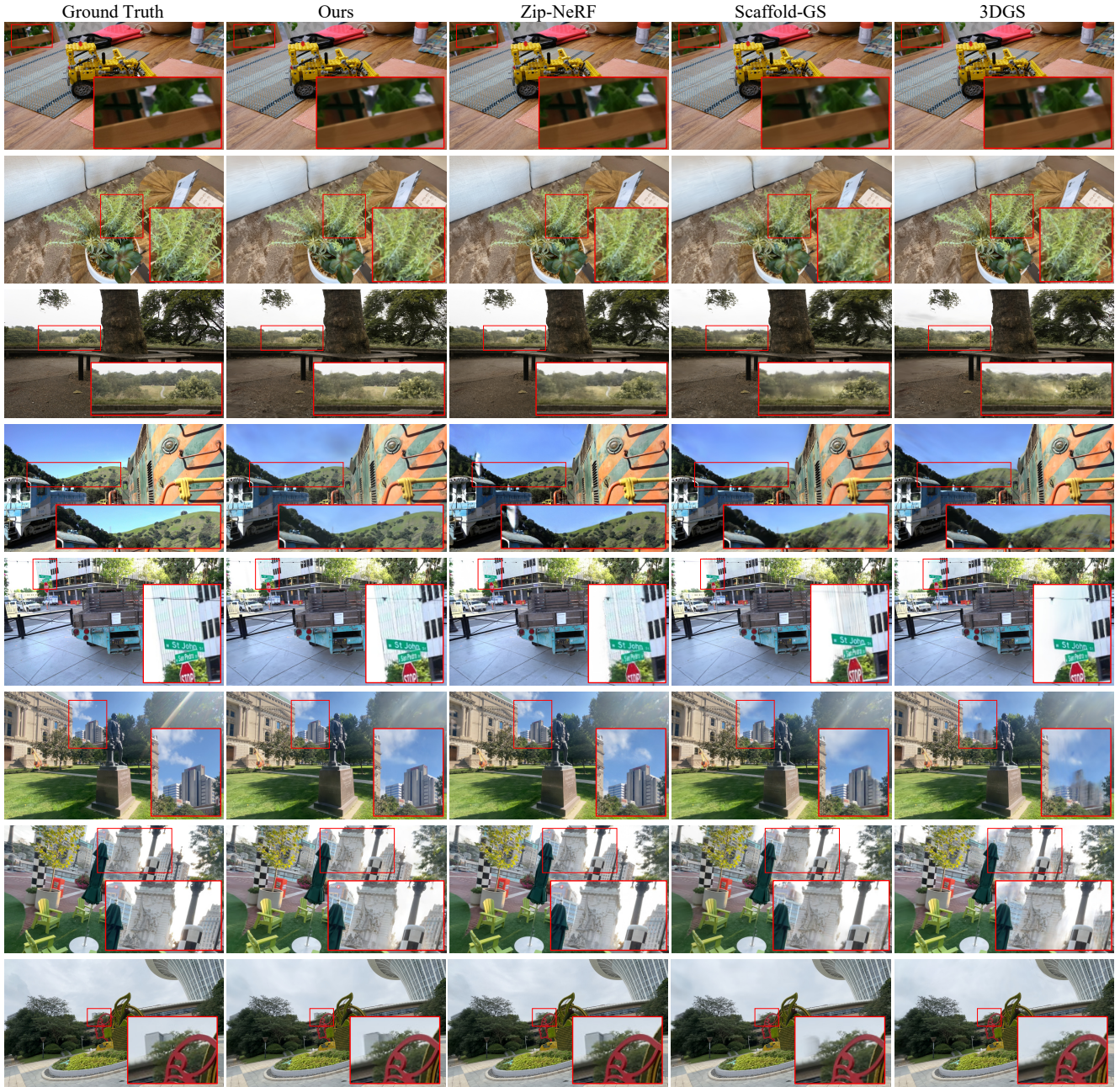


Figure 4. **Visual comparisons on novel view synthesis.** We show comparisons of our method with previous methods on test views. The figure includes KITCHEN and TREEHILL from the Mip-NeRF360 dataset; TRAIN and TRUCK from Tanks&Temples; and scenes 21, 26, 69, and 97 from the DL3DV benchmark. The top two rows highlight close-up details in indoor scenes, while the following rows showcase fine details in distant outdoor scenes. Key differences in quality are highlighted by insets.

point in Cartesian coordinates corresponds to a line through the origin in homogeneous coordinates, where any non-zero point along this line maps to the same Cartesian coordinate. Consequently, setting  $w$  to  $1/d$  at initialization is merely a particular solution rather than a strict requirement.

**Increasing the Number of Points.** We observe an increase in the number of points in our results compared to

those produced by 3DGS. To examine the effect of the increase in the number of points, we controlled the number of points in 3DGS [7] to match approximately that in ours (see 3DGS (Dense) in Table 4). Our method achieves similar performance with 3DGS (Dense) in storage, training time, and rendering FPS. Increasing the points in 3DGS does not improve its overall rendering quality and leaves its limitations in handling distant objects.

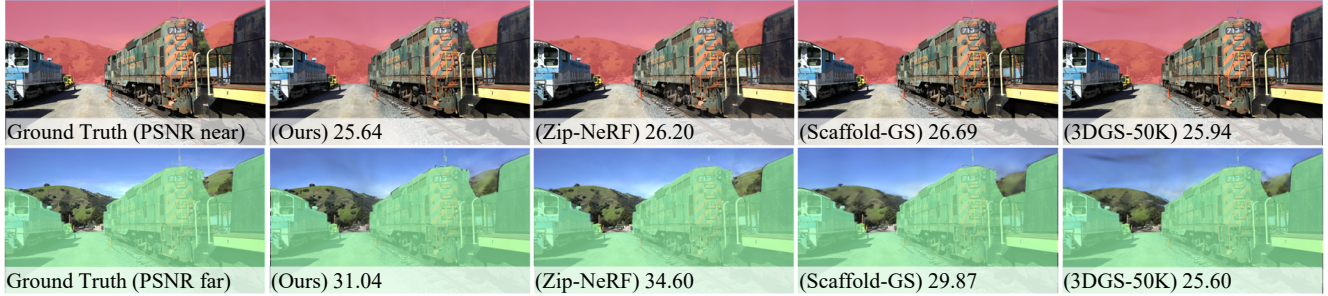


Figure 5. **Depth-wise visual comparison.** Our HoGS exhibits similar performance to 3DGS-based methods on objects close to the view, and surpasses 3DGS-based counterparts in reconstructing distant details, achieving a comparable result to Zip-NeRF.

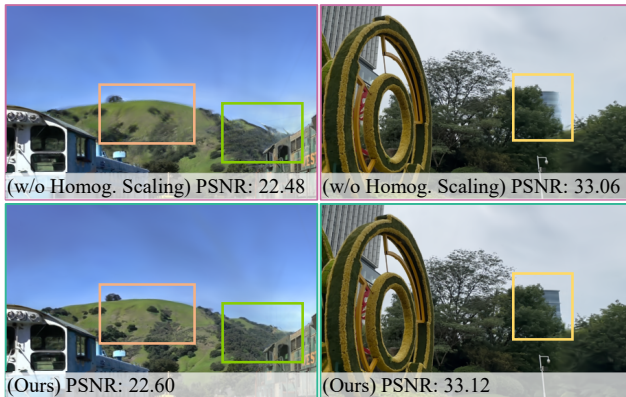


Figure 6. **Ablation for homogeneous scaling.** Without homogeneous scaling, distant details become blurry as Gaussians fail to capture the precise shape of distant objects. This limitation leads to a loss of clarity in remote regions, causing indistinct contours and inaccurate representations of fine details, which diminishes the overall realism of the rendered scene.

Method	# of points	PSNR <sup>†</sup>	PSNR (Far) <sup>†</sup>	Storage [MB]	Training [s]	Rendering FPS
3DGS	1,030,961	26.06	31.63	244	1,080	289
3DGS (Dense)	1,338,143	25.98	32.09	319	1,160	212
HoGS (Ours)	1,322,574	27.74	35.78	333	1,260	239

Table 4. Average performance comparisons between 3DGS and HoGS on TRAIN, and DL3DV scene 69 and 97.

## 5. Conclusions

We have proposed Homogeneous Gaussian Splatting (HoGS), the first approach to integrating homogeneous representations into 3DGS, which provides a remarkable improvement on 3DGS via ultimately simple implementation. Leveraging the strength of homogeneous representations, HoGS enables realistic reconstruction for both near and far objects, where original (*i.e.*, Cartesian) 3DGS often fails to represent far objects. Despite its simplicity, HoGS’s novel view rendering accuracy achieves mostly the best among 3DGS-based methods including those using complex pre-computation like scene segmentation. Rather, HoGS’s accuracy nearly reaches the state-of-the-art of time-consuming NeRF-based baselines while preserving 3DGS’s real-time rendering capability.

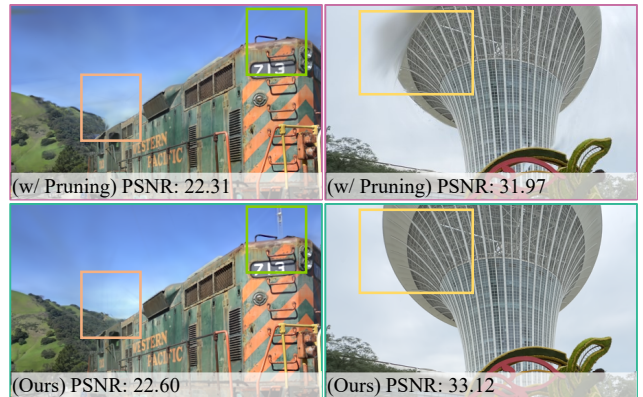


Figure 7. **Ablation for the modification on pruning strategy.** The removal of large-diameter Gaussians in world space results in the exclusion of specific distant Gaussian components. Consequently, nearby floaters approximate distant details. These floaters cannot precisely capture the structure and texture of distant regions. This substitution leads to distortions in some viewpoints, producing unrealistic renderings and insufficient detail representation in distant areas.

**Limitations.** Our method partly inherits the limitation of the original 3DGS and other 3D reconstruction methods. It is challenging to reconstruct regions that are not well observed, leading to artifacts in the same manner as the previous methods do. Since our method inherits the visibility algorithm from 3DGS, it can cause abrupt changes in the depth ordering of Gaussians.

Compared to the original 3DGS, our method preserves large Gaussians in world space and optimizes distant Gaussians to capture background details. This can be computationally intensive in scenes with high-frequency background details, as a result of densification. As shown in Table 4, our method increases the average number of points by 28.3% compared to the original 3DGS, which lead to higher memory and storage consumption.

**Acknowledgments.** This work was partially supported by JSPS KAKENHI Grant JP23H05491 and JST FOREST Grant JPMJFR206F.

## References

- [1] Jonathan T. Barron, Ben Mildenhall, Matthew Tancik, Peter Hedman, Ricardo Martin-Brualla, and Pratul P. Srinivasan. Mip-NeRF: A multiscale representation for anti-aliasing neural radiance fields. In *Proceedings of IEEE/CVF International Conference on Computer Vision (ICCV)*, 2021. 2
- [2] Jonathan T. Barron, Ben Mildenhall, Dor Verbin, Pratul P. Srinivasan, and Peter Hedman. Mip-NeRF 360: Unbounded anti-aliased neural radiance fields. In *Proceedings of IEEE/CVF Conference on Computer Vision and Pattern Recognition (CVPR)*, 2022. 2, 5, 6, 3
- [3] Jonathan T. Barron, Ben Mildenhall, Dor Verbin, Pratul P. Srinivasan, and Peter Hedman. Zip-NeRF: Anti-aliased grid-based neural radiance fields. In *Proceedings of IEEE/CVF International Conference on Computer Vision (ICCV)*, 2023. 2, 5, 6
- [4] Anpei Chen, Zexiang Xu, Andreas Geiger, Jingyi Yu, and Hao Su. TensorRF: Tensorial radiance fields. In *Proceedings of European Conference on Computer Vision (ECCV)*, 2022. 2
- [5] Minglin Chen, Longguang Wang, Yinjie Lei, Zilong Dong, and Yulan Guo. Learning spherical radiance field for efficient 360° unbounded novel view synthesis. *IEEE Transactions on Image Processing (TIP)*, 33:3722–3734, 2024. 2
- [6] Sara Fridovich-Keil, Alex Yu, Matthew Tancik, Qinhong Chen, Benjamin Recht, and Angjoo Kanazawa. Plenoxels: Radiance fields without neural networks. In *Proceedings of IEEE/CVF Conference on Computer Vision and Pattern Recognition (CVPR)*, 2022. 2
- [7] Bernhard Kerbl, Georgios Kopanas, Thomas Leimkühler, and George Drettakis. 3D Gaussian splatting for real-time radiance field rendering. *ACM Transactions on Graphics (TOG)*, 42(4):139:1–139:14, 2023. 1, 2, 3, 5, 6, 7
- [8] Bernhard Kerbl, Andreas Meuleman, Georgios Kopanas, Michael Wimmer, Alexandre Lanvin, and George Drettakis. A hierarchical 3D gaussian representation for real-time rendering of very large datasets. *ACM Transactions on Graphics (TOG)*, 43(4):62:1–62:15, 2024. 2, 3
- [9] Arno Knapitsch, Jaesik Park, Qian-Yi Zhou, and Vladlen Koltun. Tanks and temples: Benchmarking large-scale scene reconstruction. *ACM Transactions on Graphics (TOG)*, 36(4):78:1–78:13, 2017. 5, 2, 3, 6
- [10] Jonas Kulhanek and Torsten Sattler. NerfBaselines: Consistent and reproducible evaluation of novel view synthesis methods. *arXiv:2406.17345*, 2024. 5
- [11] Lu Ling, Yichen Sheng, Zhi Tu, Wentian Zhao, Cheng Xin, Kun Wan, Lantao Yu, Qianyu Guo, Zixun Yu, Yawen Lu, et al. DL3DV-10k: A large-scale scene dataset for deep learning-based 3d vision. In *Proceedings of IEEE/CVF Conference on Computer Vision and Pattern Recognition (CVPR)*, 2024. 5, 3
- [12] Lingjie Liu, Jiatao Gu, Kyaw Zaw Lin, Tat-Seng Chua, and Christian Theobalt. Neural sparse voxel fields. In *Advances in Neural Information Processing Systems (NeurIPS)*, 2020. 2
- [13] Tao Lu, Mulin Yu, Linning Xu, Yuanbo Xiangli, Limin Wang, Dahua Lin, and Bo Dai. Scaffold-GS: Structured 3D gaussians for view-adaptive rendering. In *Proceedings of IEEE/CVF Conference on Computer Vision and Pattern Recognition (CVPR)*, 2024. 2, 5, 6
- [14] Ben Mildenhall, Pratul P. Srinivasan, Matthew Tancik, Jonathan T. Barron, Ravi Ramamoorthi, and Ren Ng. NeRF: Representing scenes as neural radiance fields for view synthesis. In *Proceedings of European Conference on Computer Vision (ECCV)*, 2020. 1, 2
- [15] Thomas Müller, Alex Evans, Christoph Schied, and Alexander Keller. Instant neural graphics primitives with a multiresolution hash encoding. *ACM Transactions on Graphics (TOG)*, 41(4):102:1–102:15, 2022. 2, 5, 6
- [16] Thomas Neff, Pascal Stadlbauer, Mathias Parger, Andreas Kurz, Joerg H. Mueller, Chakravarty R. Alla Chaitanya, Anton S. Kaplanyan, and Markus Steinberger. DOnERF: Towards real-time rendering of compact neural radiance fields using depth oracle networks. *Computer Graphics Forum*, 40(4):45–59, 2021. 2
- [17] Christian Reiser, Songyou Peng, Yiyi Liao, and Andreas Geiger. KiloNeRF: Speeding up neural radiance fields with thousands of tiny MLPs. In *Proceedings of IEEE/CVF International Conference on Computer Vision (ICCV)*, 2021. 2
- [18] Hannah Schieber, Jacob Young, Tobias Langlotz, Stefanie Zollmann, and Daniel Roth. Semantics-controlled gaussian splatting for outdoor scene reconstruction and rendering in virtual reality. In *Proceedings of IEEE Conference on Virtual Reality and 3D User Interfaces (VR)*, 2024. 2
- [19] Qiangeng Xu, Zexiang Xu, Julien Philip, Sai Bi, Zhixin Shu, Kalyan Sunkavalli, and Ulrich Neumann. PointNeRF: Point-based neural radiance fields. In *Proceedings of IEEE/CVF Conference on Computer Vision and Pattern Recognition (CVPR)*, 2022. 2
- [20] Zhiwen Yan, Weng Fei Low, Yu Chen, and Gim Hee Lee. Multi-scale 3D gaussian splatting for anti-aliased rendering. In *Proceedings of IEEE/CVF Conference on Computer Vision and Pattern Recognition (CVPR)*, 2024. 5, 6
- [21] Lihe Yang, Bingyi Kang, Zilong Huang, Zhen Zhao, Xiaogang Xu, Jiashi Feng, and Hengshuang Zhao. Depth Anything v2. In *Advances in Neural Information Processing Systems (NeurIPS)*, 2024. 5, 4
- [22] Chongjie Ye, Yinyu Nie, Jiahao Chang, Yuantao Chen, Yihao Zhi, and Xiao Guang Han. GauStudio: A modular framework for 3D gaussian splatting and beyond. *arXiv:2403.19632*, 2024. 2, 3
- [23] Zehao Yu, Anpei Chen, Binbin Huang, Torsten Sattler, and Andreas Geiger. Mip-splatting: Alias-free 3D gaussian splatting. In *Proceedings of IEEE/CVF Conference on Computer Vision and Pattern Recognition (CVPR)*, 2024. 5, 6
- [24] Kai Zhang, Gernot Riegler, Noah Snavely, and Vladlen Koltun. NeRF++: Analyzing and improving neural radiance fields. *arXiv:2010.07492*, 2020. 2

# HoGS: Unified Near and Far Object Reconstruction via Homogeneous Gaussian Splatting

## Supplementary Material

This supplementary material first provides a detailed comparison of our homogeneous representation with existing inverted spherical representation [24] (Sec. A). We also analyze the methods’ convergence behavior (Sec. B) and potential design choices in methods and experiments (Sec. C). An experiment in Sec. D assesses whether our method can represent an *infinitely* far object (*i.e.*, the Moon) in our dataset. Finally, Sec. E shows additional and detailed results in each scene we tested.

The supplementary video visualizes the results in a more intuitive manner, and we strongly encourage the reader to refer to it.

### A. Inverted Spherical vs. Homogeneous Representations

Similar to the homogeneous representation, the inverted spherical representation in NeRF++ [24] is also designed to represent distant objects effectively. We compare the performance of inverted spherical and homogeneous representation in 3D scene representation.

**Inverted Spherical Representation [24].** We define a point  $\mathbf{p} = [x, y, z]^T \in \mathbb{R}^3$  to be represented with the inverted spherical representation  $\mathbf{p}' = [\theta, \phi, w']^T$  as:

$$\begin{cases} \theta = \arctan\left(\frac{y}{x}\right), \\ \phi = \arcsin\left(\frac{z}{\|\mathbf{r}\|}\right), \\ w' = \frac{1}{r}, \end{cases} \quad (\text{S1})$$

where  $w'$  is the inverted depth and  $r = \sqrt{x^2 + y^2 + z^2} > 1$ . The inverted spherical representation can be converted to Cartesian by:

$$\begin{cases} x = \frac{\sin \phi \cos \theta}{w'}, \\ y = \frac{\sin \phi \sin \theta}{w'}, \\ z = \frac{\cos \phi}{w'}. \end{cases} \quad (\text{S2})$$

**Comparison Results.** The quantitative results presented in Table S1 and Table S2 show that homogeneous representation consistently outperforms inverted spherical representation in indoor and near-object scenarios. Although inverted depth  $w'$  effectively represents distant points in its range  $(0, 1]$ , its mapping of points with depth within 1 to its range  $[1, +\infty)$  hinders the performance on nearby objects. In contrast, homogeneous coordinates offer a balanced representation of near and far objects, using the weight  $w$  to account for depths.

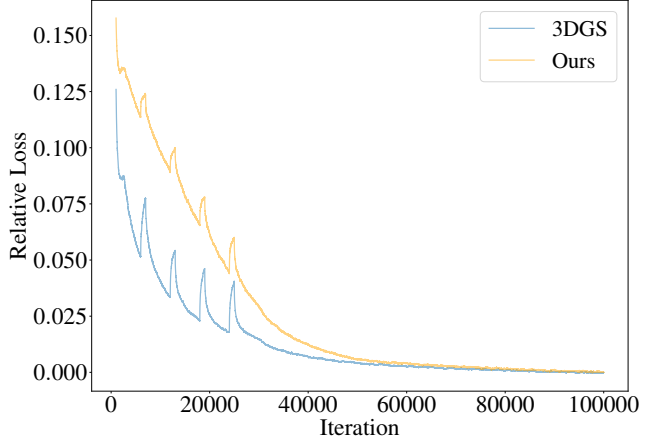


Figure S1. **Loss convergence of 3DGS and HoGS.** The loss curves indicate that with our setup on unbounded scenes, both 3DGS and HoGS have not fully converged by 30,000 iterations, while with 50,000 iterations they become nearly minimal.

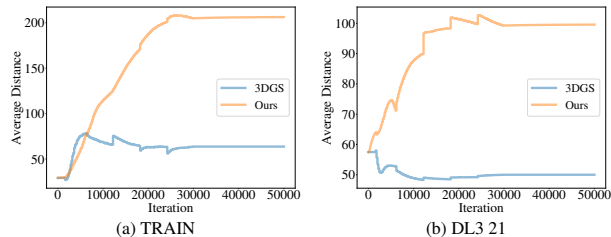


Figure S2. **Average distance of 10% farthest points.** In both the TRAIN and DL3DV 21 scenes, the 10% farthest points in our method reach significantly farther distances compared to 3DGS. By the end of the training, the farthest points in our method reach approximately 1,200 meters in the TRAIN dataset (compared to 410 meters in 3DGS) and 520 meters in DL3 Scene 21 (compared to 97 meters in 3DGS) in the physical space.

### B. More Convergence Analysis

While the main paper presents a convergence analysis in a simple setup, we further analyze the convergence behaviors.

**Extended Training.** The main paper uses 50,000 iterations for both the original 3DGS and our HoGS. To validate the number of iterations for unbounded scenes, we present the training process of 100,000 iterations in an unbounded scene (the TRAIN scene in the Tank&Temples dataset [9]) in Fig. S1. The loss curves in Fig. S1 show the relative loss, where the loss values are normalized by setting the loss at 50,000 iterations as the reference point. Both 3DGS and

Dataset Method   Metric	Mip-NeRF 360 Dataset			Tanks&Temples			DL3DV-10K Benchmark		
	SSIM <sup>↑</sup>	PSNR <sup>↑</sup>	LPIPS <sup>↓</sup>	SSIM <sup>↑</sup>	PSNR <sup>↑</sup>	LPIPS <sup>↓</sup>	SSIM <sup>↑</sup>	PSNR <sup>↑</sup>	LPIPS <sup>↓</sup>
Inverted Spherical	<b>0.828</b>	<b>27.93</b>	0.196	0.855	24.15	0.169	0.918	29.85	0.117
HoGS (Ours)	<b>0.828</b>	27.92	<b>0.194</b>	<b>0.858</b>	<b>24.27</b>	<b>0.166</b>	<b>0.919</b>	<b>29.93</b>	<b>0.114</b>

Table S1. **Inverted spherical vs. homogeneous representations.** This table reports the performance of Inverted Spherical and Homogeneous (HoGS) methods on three datasets: Mip-NeRF 360 [2], Tanks&Temples [9], and DL3DV-10K Benchmark [11]. Results are evaluated using three metrics: SSIM, PSNR, and LPIPS. HoGS consistently shows competitive or better performance across all datasets.

Method	Tanks&Temples (Near)			Tanks&Temples (Far)		
	SSIM <sup>↑</sup>	PSNR <sup>↑</sup>	LPIPS <sup>↓</sup>	SSIM <sup>↑</sup>	PSNR <sup>↑</sup>	LPIPS <sup>↓</sup>
Inverted Spherical	0.882	25.54	0.137	<b>0.976</b>	<b>30.78</b>	0.032
HoGS (Ours)	<b>0.883</b>	<b>25.69</b>	<b>0.135</b>	<b>0.976</b>	30.77	<b>0.031</b>

Method	DL3DV-10K (Near)			DL3DV-10K (Far)		
	SSIM <sup>↑</sup>	PSNR <sup>↑</sup>	LPIPS <sup>↓</sup>	SSIM <sup>↑</sup>	PSNR <sup>↑</sup>	LPIPS <sup>↓</sup>
Inverted Spherical	0.926	30.46	0.101	<b>0.993</b>	40.43	<b>0.013</b>
HoGS (Ours)	<b>0.927</b>	<b>30.53</b>	<b>0.098</b>	<b>0.993</b>	<b>40.55</b>	<b>0.013</b>

Method	Mip-NeRF360 (Indoor)			Mip-NeRF360 (Outdoor)		
	SSIM <sup>↑</sup>	PSNR <sup>↑</sup>	LPIPS <sup>↓</sup>	SSIM <sup>↑</sup>	PSNR <sup>↑</sup>	LPIPS <sup>↓</sup>
Inverted Spherical	0.917	30.40	<b>0.157</b>	0.746	25.13	0.223
HoGS (Ours)	<b>0.930</b>	<b>31.38</b>	0.163	<b>0.747</b>	<b>25.14</b>	<b>0.219</b>

Table S2. **Performance of inverted spherical and homogeneous methods across different scenarios.** This table highlights the performance of Homogeneous and Spherical representations on Tanks&Temples, DL3DV-10K, and Mip-NeRF360 datasets. Homogeneous representation consistently outperforms the inverted Spherical representation in indoor and near-object scenarios.

our method reduce the training losses until around 50,000 iterations, which are almost converging there, demonstrating that 50,000 iterations are reasonable for unbounded scene reconstruction in the main paper’s experiments.

**Convergence Behavior in Real Scenes.** Here, we analyze the convergence behaviors in real scenes by tracking the average displacement of the Gaussian centers farthest 10% from the world origin over iterations. Figure S2 show that far points in our method move more quickly to distant positions than the original 3DGS in unbounded scenes (TRAIN [9] and DL3DV Scene 21 [11]), underscoring the efficiency of our approach in reconstructing distant objects.

**PSNR Convergence Analysis.** We also show a PSNR-iteration curve comparing HoGS and 3DGS as shown in Fig. S3. HoGS shows a slower initial convergence due to the homogeneous optimization of near and far objects, which requires Gaussians to propagate across the entire scene. However, as training progresses, HoGS surpasses 3DGS in PSNR, demonstrating superior reconstruction fidelity and global consistency.

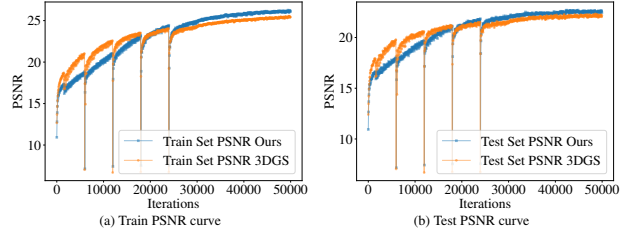


Figure S3. PSNR-iteration curve of our HoGS and 3DGS. HoGS exhibits a slower initial convergence due to the homogeneous optimization of near and far objects, requiring Gaussians to propagate across the scene. However, as training progresses, HoGS surpasses 3DGS in PSNR, demonstrating its superior reconstruction fidelity and global consistency.

## C. More Design Choices

### C.1. Skybox Initialization

Following the methods in [8, 22], we can essentially use skybox [8] initialization to enhance the points in distant scenes and the 3DGS and our proposed methods. We thus test the skybox initialization to both the 3DGS and our proposed methods. Specifically, we added 100,000 blue points as initial points on the upper hemisphere, with a radius of 1,000 unit distance, which corresponds to approximately 1.1 kilometers in DL3DV Scene 21 (estimated using the base width of the George Washington statue in front of the Indiana Statehouse) and 2.1 kilometers in the TRAIN dataset (estimated from the width of railway tracks). As shown in Table S3, the results indicate that incorporating a skybox improves the accuracy of distant scenes in the 3DGS method. This enhancement arises because the skybox provides additional guidance for representing distant elements like clouds, otherwise challenging for 3DGS to capture.

In contrast, adding a skybox to our method does not improve the accuracy of distant scenes. This is because our approach, even without skybox initialization, effectively leverages the attributes of homogeneous coordinates to represent both near and distant objects equally. Our method accurately represents distant areas without additional priors by inherently keeping consistent scaling across varying depths.

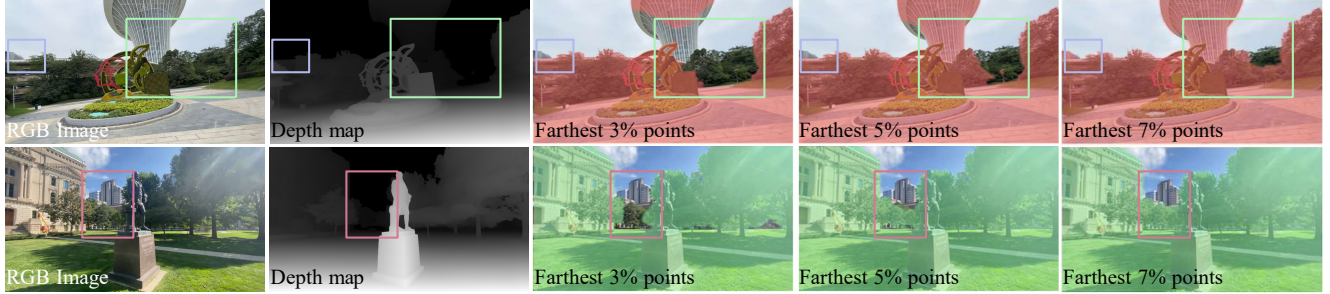


Figure S4. **Impact of threshold selection on near and far object classification.** We evaluate the effects of changing the threshold used to classify far and near objects in the depth mask used for the experiment. When the threshold is reduced to 3%, near objects such as parts of buildings and shrubs (green bounding box) and park trees (red bounding box) are mistakenly classified as far. Conversely, increasing the threshold to 7% results in some far objects, like distant buildings, being misclassified as near, as shown by the blue bounding box. To balance accuracy and meaningful far-object coverage, we select the 5 % threshold as the optimal trade-off.



Figure S5. **Reconstruction of an infinitely far (i.e., the Moon) scene.** With a 20x increase in the learning rate ( $lr$ ), our method successfully represents the Moon, even at its (near-)infinity distances, as highlighted by the red bounding box. In contrast, 3DGS fails to achieve similar results, even when the  $lr$  is largely increased, or when incorporating a skybox with different (1, 000 and 100, 000) unit distances. Notably, while adding a skybox to 3DGS improves the fidelity of cloud details compared to simply increasing  $lr$ , it remains incapable of generating a realistic appearance of the Moon.

Method	TRAIN (Near)			TRAIN (Far)		
	SSIM <sup>↑</sup>	PSNR <sup>↑</sup>	LPIPS <sup>↓</sup>	SSIM <sup>↑</sup>	PSNR <sup>↑</sup>	LPIPS <sup>↓</sup>
3DGS w/o skybox	<b>0.854</b>	<b>23.86</b>	0.151	0.960	28.49	0.063
3DGS w/ skybox	0.851	23.67	0.153	0.962	28.58	0.063
Ours w/o skybox	<b>0.854</b>	23.70	<b>0.147</b>	<b>0.976</b>	<b>30.42</b>	<b>0.044</b>
Ours w/ skybox	0.849	23.33	0.149	0.975	30.23	0.046

Method	DL3DV Scene 21 (Near)			DL3DV Scene 21 (Far)		
	SSIM <sup>↑</sup>	PSNR <sup>↑</sup>	LPIPS <sup>↓</sup>	SSIM <sup>↑</sup>	PSNR <sup>↑</sup>	LPIPS <sup>↓</sup>
3DGS w/o skybox	0.870	27.72	0.147	0.972	31.23	0.042
3DGS w/ skybox	0.867	27.78	0.152	0.976	32.16	0.038
Ours w/o skybox	0.889	28.81	0.122	<b>0.986</b>	<b>35.48</b>	<b>0.022</b>
Ours w/ skybox	<b>0.890</b>	<b>28.83</b>	<b>0.120</b>	<b>0.986</b>	35.15	<b>0.022</b>

Table S3. **Impact of skybox on near and far scenarios.** This table compares the performance of 3DGS and our method (w/ and w/o skybox) on TRAIN and DL3DV Scene 21 datasets across Near and Far scenarios. Incorporating a skybox initialization can slightly improve the accuracy of distant scenes in the original 3DGS method but not in our method. Our method effectively represents both near and far objects even without skybox initialization.

## C.2. Threshold for Near vs. Far in Experiment

In the main paper’s experiment, to evaluate the accuracy for near and far objects, we use Depth Anything V2 [21] to gen-

Scene	Threshold	Near			Far		
		SSIM <sup>↑</sup>	PSNR <sup>↑</sup>	LPIPS <sup>↓</sup>	SSIM <sup>↑</sup>	PSNR <sup>↑</sup>	LPIPS <sup>↓</sup>
TRAIN	7 %	0.858	23.82	0.143	0.972	29.94	0.048
	5 %	0.854	23.70	0.147	0.976	30.43	0.044
	3 %	<b>0.848</b>	<b>23.53</b>	0.151	<b>0.982</b>	<b>31.25</b>	<b>0.039</b>
DL3DV Scene 21	7 %	0.893	29.08	0.118	0.982	34.37	0.025
	5 %	0.889	28.81	0.122	0.986	35.48	0.022
	3 %	0.885	28.60	0.125	0.989	36.80	0.019
DL3DV Scene 97	7 %	0.965	34.63	0.047	0.989	38.69	0.043
	5 %	0.962	34.12	0.051	0.992	40.41	0.039
	3 %	0.959	33.72	0.054	0.995	42.48	0.036

Table S4. **Impact of depth threshold selection on near and far object accuracy.** This table evaluates the performance of near and far objects across different depth thresholds (7 %, 5 %, and 3 %) on the TRAIN, DL3DV Scene 21, and DL3DV Scene 97 datasets. As the threshold decreases, the accuracy for far objects consistently improves (e.g., PSNR increases from 29.94 to 31.25 on TRAIN and from 34.37 to 36.80 on DL3DV Scene 21), driven by a greater share of sky pixels characterized by uniform colors and high accuracy. However, this improvement in the metrics does not take what we really want to evaluate, e.g., buildings and mountains, into account.

erate depth maps from input images at their original resolution. We define distant areas as these maps’ farthest 5 % of

Method	BICYCLE			FLOWERS			GARDEN			STUMP			TREEHILL		
	SSIM <sup>↑</sup>	PSNR <sup>↑</sup>	LPIPS <sup>↓</sup>	SSIM <sup>↑</sup>	PSNR <sup>↑</sup>	LPIPS <sup>↓</sup>	SSIM <sup>↑</sup>	PSNR <sup>↑</sup>	LPIPS <sup>↓</sup>	SSIM <sup>↑</sup>	PSNR <sup>↑</sup>	LPIPS <sup>↓</sup>	SSIM <sup>↑</sup>	PSNR <sup>↑</sup>	LPIPS <sup>↓</sup>
3DGS	0.770	25.59	0.219	0.609	21.36	0.347	0.869	27.68	0.110	0.775	26.66	0.223	0.649	22.63	0.332
Scaffold-GS	0.768	25.57	0.228	0.610	21.67	0.337	0.869	<b>27.92</b>	0.111	0.777	26.88	0.228	<b>0.664</b>	<b>23.53</b>	0.312
HoGS (Ours)	<b>0.790</b>	<b>25.84</b>	<b>0.183</b>	<b>0.638</b>	<b>22.18</b>	<b>0.311</b>	<b>0.874</b>	27.83	<b>0.098</b>	<b>0.785</b>	<b>26.92</b>	<b>0.195</b>	0.649	22.95	<b>0.310</b>

Method	BONSAI			COUNTER			KITCHEN			ROOM		
	SSIM <sup>↑</sup>	PSNR <sup>↑</sup>	LPIPS <sup>↓</sup>	SSIM <sup>↑</sup>	PSNR <sup>↑</sup>	LPIPS <sup>↓</sup>	SSIM <sup>↑</sup>	PSNR <sup>↑</sup>	LPIPS <sup>↓</sup>	SSIM <sup>↑</sup>	PSNR <sup>↑</sup>	LPIPS <sup>↓</sup>
3DGS	0.946	32.28	0.178	0.914	29.33	0.182	0.931	31.41	0.115	0.925	31.93	0.198
Scaffold-GS	<b>0.950</b>	<b>33.08</b>	0.169	<b>0.919</b>	<b>29.81</b>	<b>0.177</b>	<b>0.934</b>	31.94	<b>0.113</b>	<b>0.932</b>	<b>32.34</b>	<b>0.181</b>
HoGS (Ours)	0.948	32.56	<b>0.164</b>	0.913	29.25	0.179	0.932	<b>32.04</b>	0.114	0.925	31.67	0.196

Table S5. **Comparisons for Mip-NeRF360 outdoor and indoor scenes.** 3DGS-based methods’ SSIM, PSNR and LPIPS scores for Mip-NeRF360 scenes. Outdoor scenes are listed above, while indoor scenes are listed below.

Dataset		Mip-NeRF 360 Dataset			Tanks&Temples			DL3DV-10K Benchmark		
Method	Metric	SSIM <sup>↑</sup>	PSNR <sup>↑</sup>	LPIPS <sup>↓</sup>	SSIM <sup>↑</sup>	PSNR <sup>↑</sup>	LPIPS <sup>↓</sup>	SSIM <sup>↑</sup>	PSNR <sup>↑</sup>	LPIPS <sup>↓</sup>
Mip-Splatting [23]		0.835	27.97	0.182	0.856	24.01	0.160	0.917	29.44	0.116
Multi-Scale 3DGS [20]		0.821	27.73	0.211	0.846	23.92	0.180	0.893	28.23	0.148
HoGS (Ours)		0.828	27.92	0.194	0.858	24.27	0.166	0.919	29.93	0.114

Table S6. **Comparison with Mip-Splatting and Multi-Scale 3D Gaussian Splatting.**

depth values. This threshold is effective because adopting the 0 % threshold would misclassify distant mountains and buildings as near objects, evaluating far objects’ accuracy only on limited sky regions. Here, we additionally tested thresholds of 3 % and 7 % as shown in Fig. S4 and Table S4. As the threshold changes from 7 % to 5 % to 3 %, the accuracy for far objects improves. This is because the number of pixels classified as distant objects decreases while the number of pixels representing the sky remains constant. Typically characterized by uniform colors and high accuracy, the sky becomes a more significant proportion of the far-object pixels as the threshold is reduced. Consequently, the overall accuracy improves with an increasing share of sky pixels in the far-object category.

However, it is essential to note that while reducing the threshold improves the accuracy metrics, it does not measure the representation of other *distant* objects, such as mountains or buildings, which are critical for photorealistic scene reconstruction (see Fig. S4). Hence, we set a 5 % threshold in the main paper’s experiment, which provides a balanced trade-off between including enough distant objects for meaningful evaluation and avoiding the misclassification of nearby elements.

## D. Representing Infinitely Far Objects

We collected a custom dataset containing scenes with the Moon to assess the reconstruction capability of objects at *infinitely* far away<sup>1</sup>. Figure S5 shows a visual comparison. With our method, increasing the learning rate ( $lr$ ) for the weight parameter  $w$  by 20x enabled the accurate reconstruction of the Moon. In contrast, 3DGS failed to recon-

<sup>1</sup>Due to its proprietary nature, this dataset is used exclusively for experimental purposes.

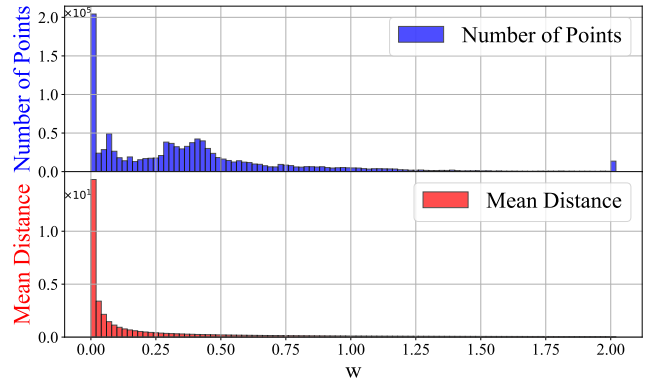


Figure S6. Histogram of  $w$ .

struct the Moon even with a large  $lr$ , with an increase of 400x, producing artifacts that disappear when the viewpoint changes. Adding a skybox with a 1,000 unit or 100,000 unit distance to 3DGS also failed to produce a realistic appearance of the Moon, where these distances are approximately 500 m and 50,000 m, respectively, in the physical space.

## E. Additional Results

We provide quantitative comparisons per scene in Tables S5–S9, and qualitative results in Figs. S7 and S8 to supplement the main paper. These include detailed figures and tables showcasing the performance of our method across various scenes.

### E.1. Distribution of $w$

We provide a histogram of the parameter  $w$  and the mean distance for each  $w$  on the TRAIN scene from

Scene	Method	Overall			Near			Far		
		SSIM <sup>↑</sup>	PSNR <sup>↑</sup>	LPIPS <sup>↓</sup>	SSIM <sup>↑</sup>	PSNR <sup>↑</sup>	LPIPS <sup>↓</sup>	SSIM <sup>↑</sup>	PSNR <sup>↑</sup>	LPIPS <sup>↓</sup>
TRAIN	3DGS	0.811	22.16	0.214	0.854	23.86	0.151	0.960	28.49	0.063
	Scaffold-GS	0.825	<b>22.69</b>	0.200	<b>0.859</b>	<b>23.87</b>	<b>0.146</b>	0.969	30.36	0.053
	HoGS (Ours)	<b>0.828</b>	22.60	<b>0.191</b>	0.854	23.70	0.147	<b>0.976</b>	<b>30.43</b>	<b>0.044</b>
TRUCK	3DGS	0.878	25.50	0.152	0.908	27.42	0.130	0.973	30.31	0.022
	Scaffold-GS	0.883	25.92	<b>0.139</b>	0.911	<b>27.87</b>	<b>0.118</b>	0.974	30.71	0.020
	HoGS (Ours)	<b>0.887</b>	<b>25.94</b>	0.141	<b>0.913</b>	27.68	0.123	<b>0.977</b>	<b>31.11</b>	<b>0.018</b>

Table S7. **Comparisons for Tanks&Temples scenes with near/far metrics.** 3DGS-based methods’ SSIM, PSNR and LPIPS scores for Tanks&Temples scenes.

Scene	Method	Overall			Near			Far		
		SSIM <sup>↑</sup>	PSNR <sup>↑</sup>	LPIPS <sup>↓</sup>	SSIM <sup>↑</sup>	PSNR <sup>↑</sup>	LPIPS <sup>↓</sup>	SSIM <sup>↑</sup>	PSNR <sup>↑</sup>	LPIPS <sup>↓</sup>
24	3DGS	0.944	31.77	0.094	0.951	32.35	0.085	0.995	41.85	0.006
	Scaffold-GS	0.946	31.98	0.090	0.950	32.32	0.084	0.997	44.33	0.003
	HoGS (Ours)	<b>0.953</b>	<b>32.70</b>	<b>0.078</b>	<b>0.955</b>	<b>32.95</b>	<b>0.075</b>	<b>0.998</b>	<b>46.82</b>	<b>0.002</b>
26	3DGS	0.904	29.48	0.185	0.911	30.13	0.176	0.994	39.67	0.007
	Scaffold-GS	0.895	29.66	0.194	0.902	30.17	0.186	0.995	40.68	0.006
	HoGS (Ours)	<b>0.913</b>	<b>30.20</b>	<b>0.165</b>	<b>0.918</b>	<b>30.64</b>	<b>0.159</b>	<b>0.996</b>	<b>41.71</b>	<b>0.005</b>
101	3DGS	0.924	27.54	0.091	0.931	27.97	0.083	0.994	39.59	0.007
	Scaffold-GS	0.907	26.94	0.106	0.911	27.20	0.102	0.997	41.01	0.003
	HoGS (Ours)	<b>0.936</b>	<b>28.26</b>	<b>0.071</b>	<b>0.939</b>	<b>28.50</b>	<b>0.068</b>	<b>0.998</b>	<b>42.40</b>	<b>0.002</b>

Table S8. **Comparisons for DL3DV Benchmark indoor scenes.** 3DGS-based methods’ SSIM, PSNR and LPIPS scores for DL3DV Benchmark indoor scenes.

Tanks & Temples [9]. indicates that  $w$  correctly converges to small values (*i.e.*,  $w \sim 0$ ) for distant scenes, and *vice versa*.

## E.2. Comparison with Mip-Splatting and Multi-Scale 3D Gaussian Splatting

We provide a comparison with 3DGS-based methods [20, 23] that focus on anti-aliasing and multi-scale representations. Even with these methods, our method still maintains state-of-the-art performance across most metrics.

Scene	Method	Overall			Near			Far		
		SSIM $\uparrow$	PSNR $\uparrow$	LPIPS $\downarrow$	SSIM $\uparrow$	PSNR $\uparrow$	LPIPS $\downarrow$	SSIM $\uparrow$	PSNR $\uparrow$	LPIPS $\downarrow$
21	3DGS	0.838	25.99	0.196	0.870	27.72	0.147	0.972	31.23	0.042
	Scaffold-GS	0.846	27.00	0.181	0.866	28.11	0.148	0.983	34.11	0.028
	HoGS (Ours)	<b>0.872</b>	<b>27.80</b>	<b>0.148</b>	<b>0.889</b>	<b>28.81</b>	<b>0.122</b>	<b>0.986</b>	<b>35.48</b>	<b>0.022</b>
69	3DGS	0.858	26.41	0.165	0.891	27.77	0.131	0.972	32.83	0.027
	Scaffold-GS	0.870	27.23	0.152	0.890	28.11	0.132	0.985	35.14	0.015
	HoGS (Ours)	<b>0.888</b>	<b>27.50</b>	<b>0.129</b>	<b>0.902</b>	<b>28.19</b>	<b>0.115</b>	<b>0.990</b>	<b>36.50</b>	<b>0.010</b>
97	3DGS	0.930	29.62	0.127	0.952	32.47	0.066	0.980	33.57	0.058
	Scaffold-GS	0.945	31.82	0.099	0.956	32.87	0.056	0.991	38.81	0.042
	HoGS (Ours)	<b>0.953</b>	<b>33.12</b>	<b>0.092</b>	<b>0.962</b>	<b>34.12</b>	<b>0.051</b>	<b>0.992</b>	<b>40.41</b>	<b>0.039</b>

Table S9. **Comparisons for DL3DV Benchmark outdoor scenes.** 3DGS-based methods' SSIM, PSNR and LPIPS scores for DL3DV Benchmark outdoor scenes.

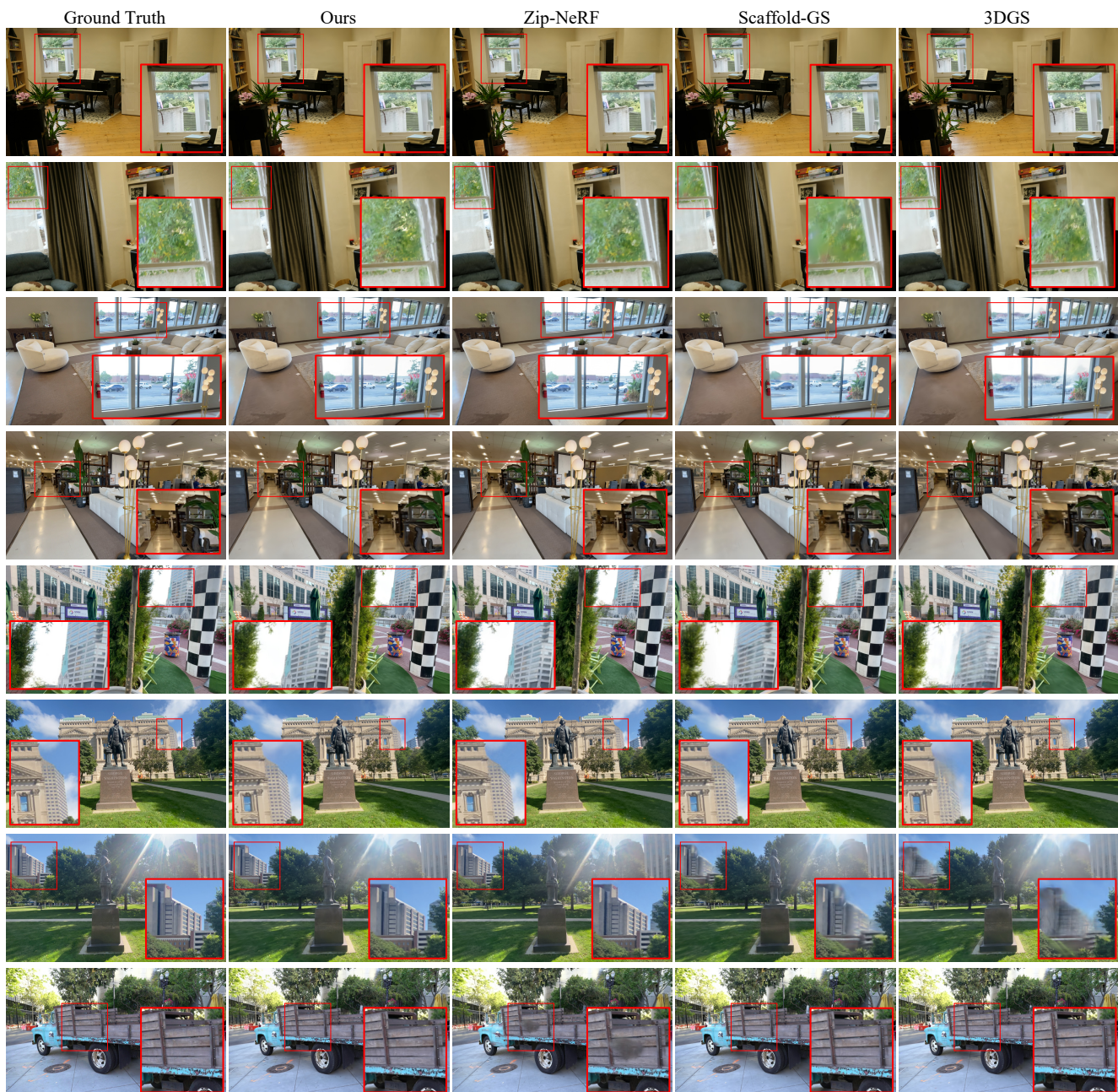


Figure S7. **Extra visual comparisons on novel view synthesis 1.** We present visual comparisons between methods on more test views. The figure includes ROOM from the Mip-NeRF360 dataset, TRUCK from Tanks&Temples, and scenes 21, 26, and 69 from the DL3DV benchmark. Key differences in quality are highlighted by insets.

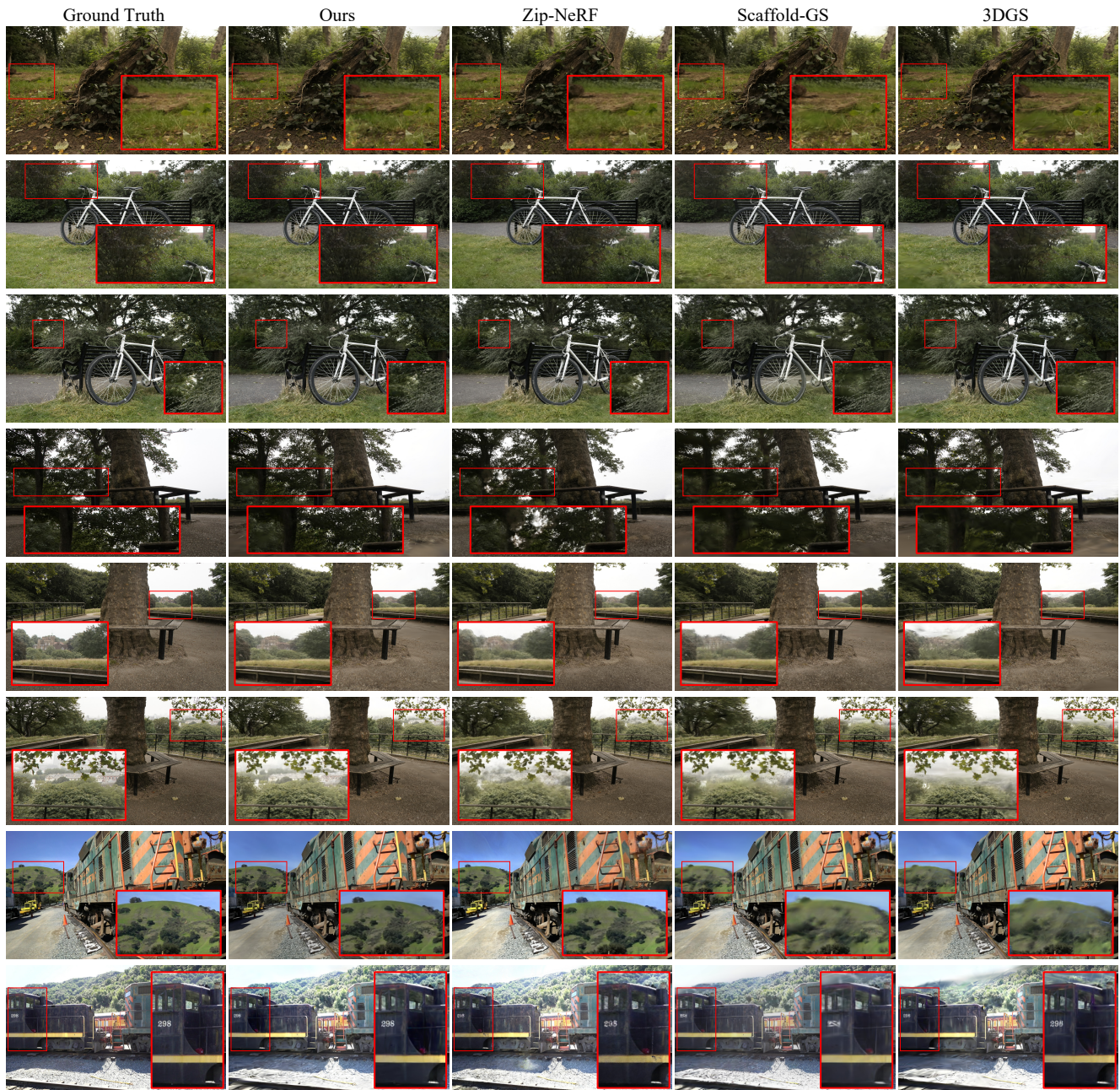


Figure S8. **Extra visual comparisons on novel view synthesis 2.** We present visual comparisons between methods on more test views. The figure includes STUMP, BICYCLE, and TREEHILL from the Mip-NeRF360 dataset; and TRAIN from Tanks&Temples. Key differences in quality are highlighted by insets.